Turbulent heat transfer in a liquid metal tube flow with azimuthally inhomogeneous heat flux

Tim Laube[a], Benjamin Dietrich[a,*], Luca Marocco[b], Thomas Wetzel[a]

[a] *Institute of Thermal Process Engineering, Karlsruhe Institute of Technology (KIT),* [1]*Kaiserstrasse 12, 76131 Karlsruhe, Germany*
[b] *Department of Energy, Politecnico di Milano,via Lambruschini 4, 20156 Milan, Italy*

ARTICLE INFO

ABSTRACT

An experimental study of the convective heat transfer in a turbulent liquid metal tube flow with azimuthally inhomogeneous heat flux is presented. Prior to the liquid metal experiments, the validation of the test section was realized using water. These results showed a very good agreement with literature data. For the liquid metal experiments, an eutectic alloy of gallium, indium and tin (GaInSn) was used. The Péclet number was varied between 1400 and 3600, thus in a regime of forced convection. Experiments with homogeneous heating over the full circumference of the tube and inhomogeneous heating over half of the circumference with the other half being insulated, were performed. The azimuthally averaged Nusselt number and the temperature distribution in the tube wall were investigated. The results suggest that the azimuthally averaged Nusselt number for water and liquid metal tube flows with inhomogeneous heating over the circumference can be calculated sufficiently well with literature correlations for uniform heat flux. For an inhomogeneous heat flux the azimuthal temperature gradient in the tube wall increases for higher Reynolds number and is more pronounced for GaInSn than for water. Furthermore, impurities like oxide particles significantly decrease the liquid metal convective heat transfer coefficient.

1. Introduction

Concentrated solar power plants (CSP) can play a major role in the upcoming transition to a more sustainable energy supply. These facilities are, in combination with an energy storage, able to provide baseload power. CSP use concentrated solar energy, to heat up a heat transfer fluid, which subsequently transfers its energy to a power cycle to produce electricity. Several authors discuss the application of liquid metals in concentrated solar power plants [2–4]. The use of these heat transfer fluids (HTFs) allow an improved overall process efficiency due to higher operating temperatures and heat flux densities at the thermal receiver compared to state-of-the-art HTFs such as solar salts or gases [4]. Experimental results of a small-scale concentrated solar power facility safely operated with liquid metal were recently published by Müller-Trefzer et al. [5] up to a peak heat flux density of 4 MW m^{-2} at the solar receiver.

The contribution of molecular heat conduction to the overall heat transfer in liquid metals ($Pr \ll 1$) is high even for turbulent flows, preventing the applicability of heat transfer correlations for

conventional fluids ($Pr \geq 0.6$) and makes problem specific experimental and numerical studies necessary [6].

Regarding a CSP plant with central receiver system design, the latter is typically made of an array of tubes. The concentrated solar light on the outside of the receiver covers only half of the circumference of the tube, leading to a strongly azimuthally inhomogeneous heat flux [7]. This kind of thermal boundary condition was sparsely studied in literature. For conventional fluids and azimuthally inhomogeneous heating, the most extensive studies are those by Schmidt et al. [8] and Chang et al. [9] for water, Black and Sparrow [10] and Knowles and Sparrow [11] for air as well as Yang et al. [12] for molten salt. They show that the azimuthally averaged Nusselt numbers for azimuthally inhomogeneous heated tube flows could be predicted by correlations developed for azimuthally homogeneous heated cases. However, these findings cannot be transferred directly to liquid metal flows, as mentioned before. For the case of turbulent liquid metal tube flows with azimuthally homogeneous heat flux, numerous studies have been performed in literature showing substantial discrepancies in the results despite similar set ups and boundary conditions. Pacio et al. [13] gathered over 1100 experimental data points from 21 authors and evaluated 15 correlations for this problem. Based on a statistical evaluation, the authors recommend specific correlations to predict the convective heat transfer coefficient for different liq-

Nomenclature

Latin symbols

a	thermal diffusivity / $\text{m}^2 \text{ s}^{-1}$
A	cross sectional area / m^2
c	coverage factor uncertainty / $-$
c_p	specific heat capacity at constant pressure / $\text{J kg}^{-1} \text{ K}^{-1}$
d	diameter thermocouple / m
D	inner diameter test section / m
g	gravitational acceleration / m s^{-2}
Gr^*	modified Grashof number [1], $= \frac{D^3 \cdot \rho \cdot g \cdot \beta}{\eta} \cdot \frac{dT}{dz} \cdot / -$
h	convective heat transfer coefficient / $\text{W m}^{-2} \text{ K}^{-1}$
i	counter variable / $-$
k	thermal conductivity / $\text{W m}^{-1}\text{K}^{-1}$
L	length / m
$\dot{M}$	mass flowrate / kg s^{-1}
n	number of measurements / $-$
Nu	Nusselt number, $= \frac{h \cdot D}{k} / -$
P	electrical power / W
Pe	Péclet number, $= \text{Re} \cdot Pr = \frac{4 \cdot \dot{M} \cdot c_p}{\pi \cdot D \cdot k} / -$
Pr	Prandtl number, $= \frac{\eta \cdot c_p}{k} / -$
$\dot{Q}$	Heat flux / W
$\dot{q}$	heat flux density / W m^{-2}
r	radial coordinate / m
Ra	Rayleigh number, $= Gr^* \cdot Pr / -$
Re	Reynolds number, $= \frac{4 \cdot \dot{M}}{\pi \cdot D \cdot \eta} / -$
s	thickness / m
T	temperature / K
u	velocity / m s^{-1}
U	extended uncertainty / $-$
$\dot{V}$	volume flowrate / $\text{m}^3 \text{ s}^{-1}$
x	referring to an arbitrary quantity
Z	mixed convection parameter [1], $= \frac{\text{Ra}}{\text{Re}} \cdot \frac{D}{L} / -$

Greek symbols

β	thermal expansion coefficient / K^{-1}
ϕ	azimuthal coordinate / $^\circ$
Θ	nondimensional temperature / $-$
ρ	density / kg m^{-3}
η	dynamic viscosity / mPa s
ν	kinematic viscosity / m^2s^{-1}

Sub-/superscripts

b	bulk temperature
Cu	copper
f	fluid
heat	heated
hom	homogeneous
hyd	hydraulic
i	inside
in	inlet
inhom	inhomogeneous
max	maximum
melt	melting point
mp	measurement plane
o	outside
out	outlet
ref	reference
res	resulting
TC	thermocouple
W	wall
z	local position in test section

Operators

$< \cdot >$	circumferential average

Abbreviations

2-D	two-dimensional
GaInSn	gallium-indium-tin
HTF	heat transfer fluid
IH	inhomogeneous heat flux
LBE	lead-bismuth-eutectic
LM	liquid metal
MAPE	mean absolute percentage error
MID	magnetic-inductive flow meter
OH	homogeneous heat flux

uid metals, with the correlation of Skupinski et al. [14] as best fit for all classes of liquid metals. In the case of an azimuthally inhomogeneous heated tube, experimental works were mainly conducted in the context of nuclear fusion technology focusing on the influence of strong magnetic fields on the flow [15–17]. They all use mercury as working fluid in combination with tubes made of stainless steel. Unfortunately, in these works, the experimental facilities are not described in detail and no uncertainties of the data are given. Marocco et al. [7] and Straub et al. [18] numerically investigated a turbulent liquid metal flow with an azimuthally varying heat flux distribution. They show that the circumferentially averaged Nusselt number of an azimuthally inhomogeneous heated liquid metal tube flow can also be predicted with correlations developed for an azimuthally homogeneous heated flow. Nevertheless, they cannot be used to predict local Nusselt numbers and wall temperatures.

Due to the lack of reliable experimental literature data for a turbulent liquid metal flow in an azimuthally inhomogeneous heated tube the present work aims at gathering accurate data for the validation of numerical simulations and to check the available Nusselt correlations for the design of engineering equipment. For this purpose, the azimuthally averaged Nusselt numbers as well as the wall temperature distributions were analysed. Particular attention was devoted to the evaluation of the temperature inside the tube wall at different Reynolds numbers, which is crucial for the conceptual design of a central receiver tube. Due to the large number of available literature data for water, the test section was first validated with this fluid. For the liquid metal flow, azimuthally homogeneous and inhomogeneous heated cases were studied and compared to available Nusselt number correlations.

2. Experimental setup

2.1. Heat transfer medium

In this work an eutectic alloy of gallium (65.9 mass%), indium (20.3 mass%) and tin (13.8 mass%) (GaInSn) called MCP 11 from 5N Plus UK Ltd. was used to perform the liquid metal heat transfer experiments. Its melting point is $T_{\text{melt}} = 10.5\ ^\circ\text{C}$, while all other properties like the kinematic viscosity ν, thermal conductivity k or specific heat capacity at constant pressure c_p are well representative for a wide range of liquid metals. This and its non-toxicity make it a suitable lab fluid [19]. Challenges are caused by its high corrosiveness against structural materials, especially at elevated temperatures [20–22], its fast oxidation even in an environment with low oxygen content [23] and a very high price.

For this work, relevant physical properties of GaInSn at $T = 25\ ^\circ\text{C}$ are summarized exemplarily in Table 1 together with the corresponding uncertainties. Except for the dynamic viscosity η, which was taken from the work of Plevachuk et al. [24], the other

Table 1
Physical properties of GaInSn

Physical property	value at $T = 25$ °C, $p = 1$ bar	uncertainty
density	$\rho = 6411.78$ kg m^{-3} [25]	±0.06%
specific heat capacity at constant pressure	$c_p = 399.85$ J kg^{-1}K^{-1} [25]	±4.18%
thermal conductivity	$k = 25.06$ W m^{-1}K^{-1} [25]	±4.22%
dynamic viscosity	$\eta = 2.1$ mPa s [24]	±3%
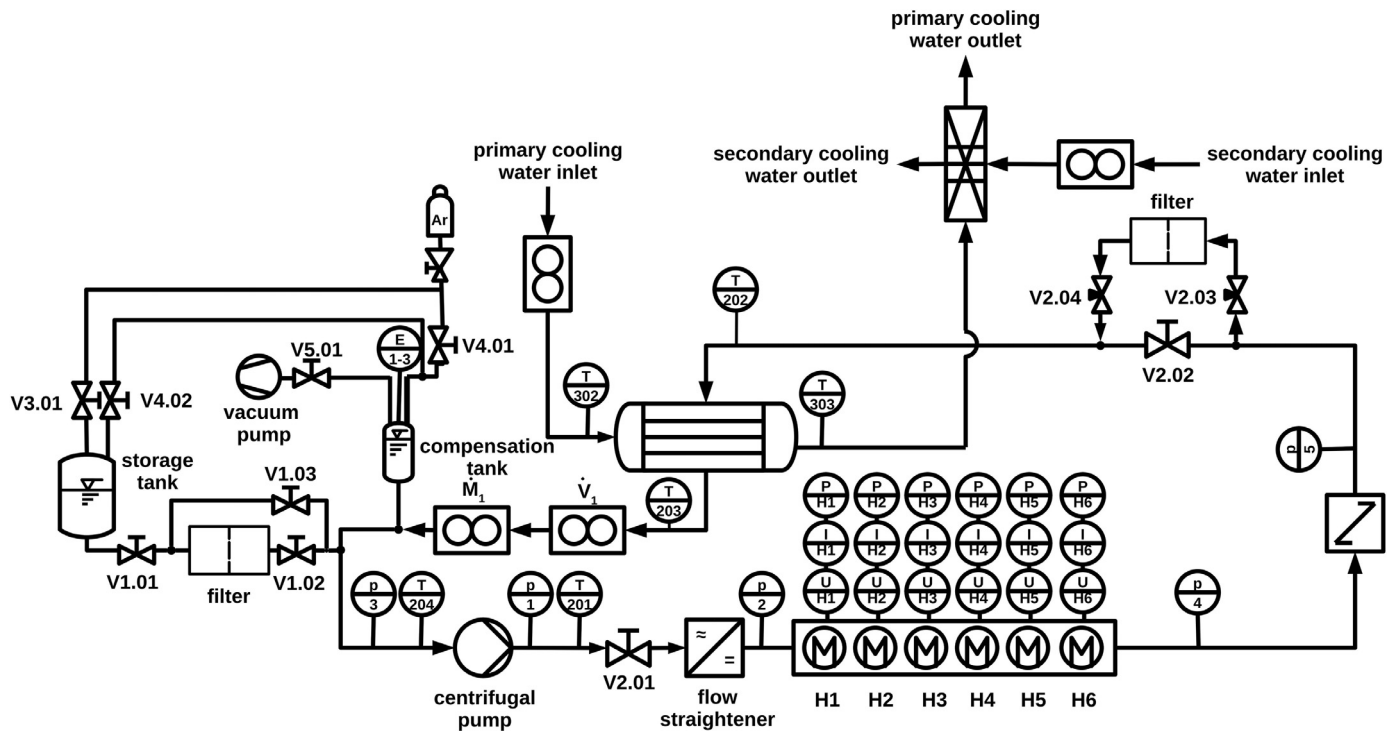
Fig. 1. Scheme of the liquid metal loop

physical properties were previously determined by the authors themselves [25].

2.2. Liquid metal test facility

The experiments were performed with a liquid metal test loop at the KArlsruhe Liquid metal LAboratory (KALLA) of the Karlsruhe Institute of Technology (KIT). This loop contains approximately 5 liters of GaInSn. The test facility comprises four individual parts, namely the liquid metal loop, the argon loop, the primary cooling water loop and the secondary cooling water loop. A scheme of the arrangement is shown in Fig. 1.

The liquid metal loop consists of a frequency-controlled centrifugal pump (Model MPN190, Schmitt) and a flow straightener to ensure a swirl-free and symmetrical velocity profile at the inlet of the test section. The horizontally arranged test section is placed behind the flow straightener. A filter (Alfred Durst Filtertechnik GmbH) with a mesh size of 20 μm is used to remove oxide particles from the liquid metal. An expansion tank equipped with a vacuum pump (Leybold GmbH) is used to compensate the thermal expansion of the fluid. A storage tank is installed, to store the liquid metal during maintenance.

The filling line from the storage tank is equipped with another filter (Alfred Durst Filtertechnik GmbH) with a mesh size of 20 μm to ensure that oxide particles, potentially being in the storage tank, do not enter the loop. To prevent oxidation of the liquid metal, an inert argon atmosphere protects both the loop and the storage tank. Prior to each filling process, oxygen is removed by applying

vacuum to the loop and flushing it with argon. This procedure is repeated three times. The loop is equipped with five pressure sensors p1-p5 (ICS Schneider Messtechnik IMP 321 and ICS Schneider Messtechnik IMP 331) to measure the absolute pressure at selected points in the loop. The operating temperatures are measured with thermocouples (TC) T201-T204 (type K, $d_{TC} = 3$ mm) at four positions and their signals are directly connected to a PLC control system (Siemens Simatic S7). The liquid metal flowrate is measured with a volumetric flow meter and a mass flow meter. The former is a magnetic-inductive flow meter $\dot{V}_1$ (Krohne Altoflux X1000 with Altometer SC100AS), whereas the latter is a coriolis mass flow meter $\dot{M}_1$ (Yokogawa Rotamass Prime 50 with measuring transducer Ultimate). Due to the lower uncertainties, the mass flowrate of all results reported in this work was determined using the coriolis flow sensor. The magnetic-inductive flow meter was only used for controll purposes. More details about the flow measurements are given in Appendix A. The test section is described in detail in Section 2.3. A shell and tube heat exchanger connected to the cooling water removes the heat dissipated in the pump and in the test section. The cooling water loop is divided in a primary and secondary loop, each consisting of one cooler (Lauda VC2000 and Lauda UC180), that are connected via a plate heat exchanger. Each loop has a magnetic inductive flow meter (Krohne Altoflux X1000 with Altometer SC100AS). The cooling water temperature at the inlet and outlet of the heat exchanger to the liquid metal is controlled with two thermocouples T302-T303 (type K, $d_{TC} = 3$ mm). Both loops are necessary to ensure a sufficiently stable cooling water temperature even at high heat loads of up to $P_{\text{heaters}} = 10$ kW
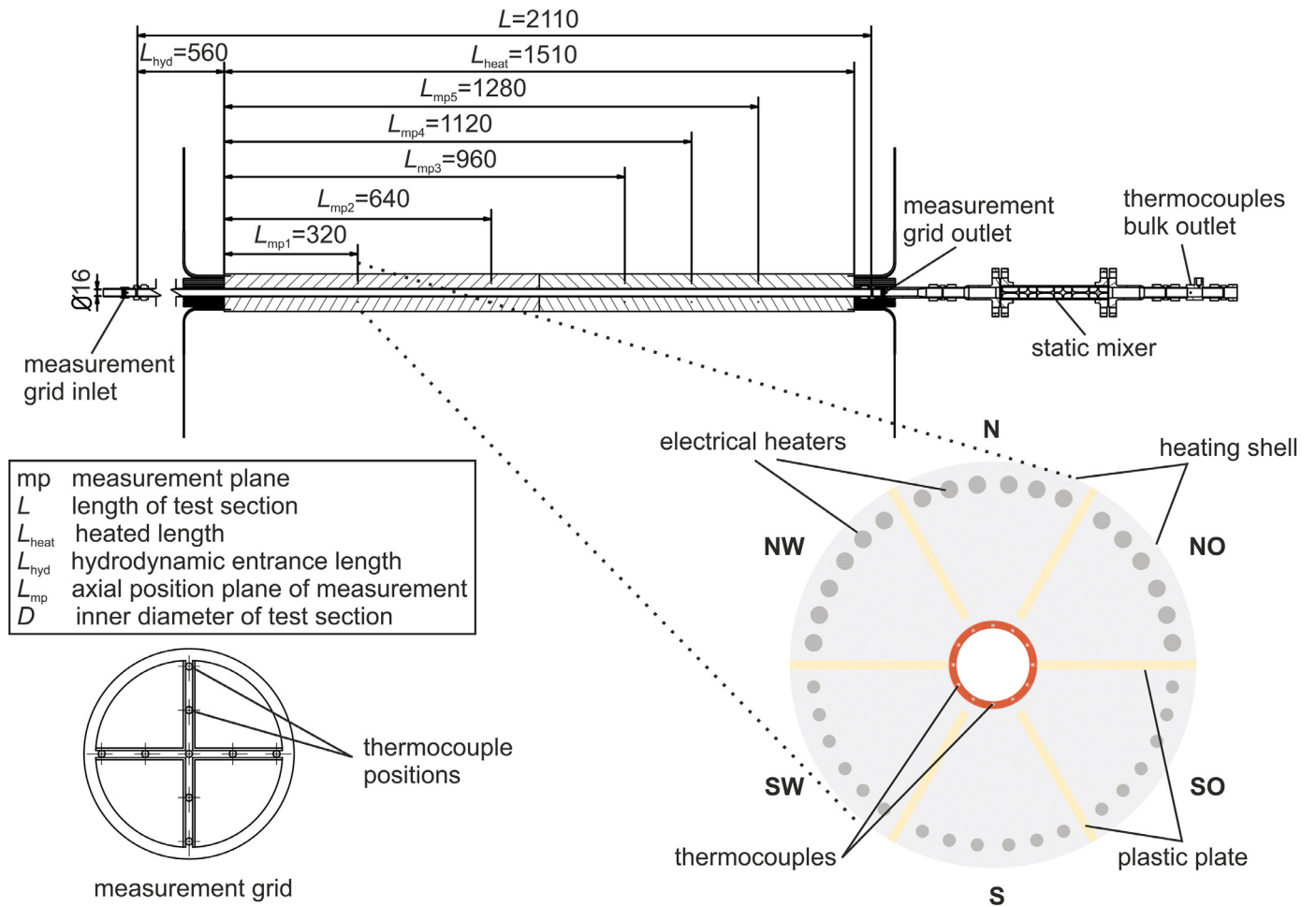
Fig. 2. Axial and cross-sectional view of the test section and measurement grid

in the test section. All sensors of the facility are also shown in the scheme of Fig. 1.

2.3. Test section

The test section is made from a copper tube (CW024A) with an inner diameter of $D = 16$ mm and a wall thickness of $s = 1.8$ mm. Copper was used due to its high thermal conductivity. Furthermore, it is compatible with GaInSn, at least for low temperatures and short usage times [20]. High heat flux densities are necessary to achieve sufficiently large temperature differences in the liquid metal, thus reducing measurement uncertainties. Moreover, the radial temperature gradient in the tube wall should be as small as possible, to allow an accurate determination of the local wall temperature. Therefore, 60 thermocouples (type K, $d_{TC} = 0.5$ mm) are allocated on five cross sectional planes at distances of $\frac{L_{mp,i}}{D} = [20, 40, 60, 70, 80]$ from the beginning of the heated section. Twelve thermocouples are positioned with an azimuthal pitch of $\Delta\phi = 30°$ at every plane. The thermocouples are soldered in axially grooves within the copper tube and the thermocouple wires are in the grooves parallel to the flow direction to minimize the influence of temperature gradients along the thermocouples on the measurement. The radial distance between the inner tube wall and the center of the thermocouples is $\Delta r = 0.75$ mm.

An axial view of the test section is shown at the top of Fig. 2. The liquid metal enters the test section from the left. The radial temperature distribution of the fluid is measured at four angular and three radial positions (see Fig. 2) with a grid consisting of nine thermocouples (type K, $d_{TC} = 0.5$ mm). After an unheated length of $L_{hyd} = 35 \cdot D = 560$ mm the flow is heated by six heating shells for $L_{heat} = 94.4 \cdot D = 1510$ mm. The electrical heaters are mortised in the heating shells. The heating can be adjusted individually for each heating shell through power controllers (Advanced Energy Thyro-PX power controller). Consequently, the heat flux can be controlled sector-wise in 60° steps.

A thermal gapfiller (HALA TEL-Z-SI) ensures a good thermal contact between the heating shells and the copper tube. Plastic plates made of polyether ether ketone are placed between the heating shells to thermally insulate each one from the others, so that the azimuthal heat flux between two neighbouring shells is minimized. At the outlet of the test section, the fluid temperature is measured with a measurement grid consisting of nine thermocouples (type K, $d_{TC} = 0.5$ mm) of the same type as at the inlet one. Additionally, the mixing temperature of the fluid is determined using a static mixing element (NOV-Kenics 1-KMS-6) and three thermocouples (type K, $d_{TC} = 1$ mm) behind it. Each thermocouple has a different insertion depth to capture the fluid temperature at several radial positions. To measure the temperature of the heating shells at every measurement plane, 30 thermocouples are positioned in bores within the heating shells with six thermocouples at each plane. To reduce heat losses to the environment, the entire test section is thoroughly insulated. 36 thermocouples (type K, $d_{TC} = 1$ mm) are positioned in the insulation and on the outer surface of the insulation layer to determine the temperatures across the insulation. Further, three thermocouples (type K, $d_{TC} = 0.5$ mm) are used to measure the ambient temperature at
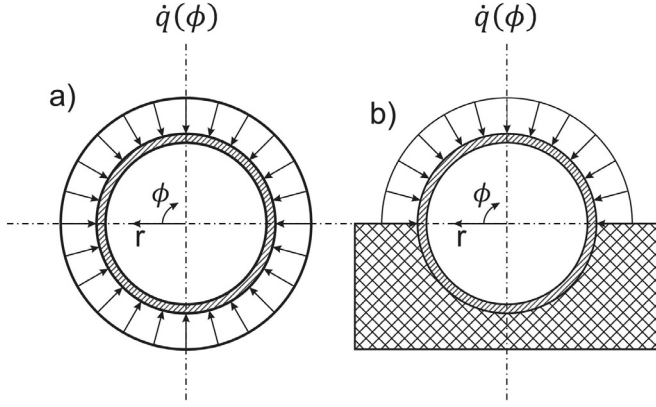
Fig. 3. Thermal boundary conditions for OH (a) and IH (b)

different positions along the loop. This allows an accurate estimation of the energy losses to the environment.

By controlling the dissipated power in the heating shells, an azimuthally homogeneous (OH) and an azimuthally inhomogeneous (IH) heat flux can be applied to the outer surface of the copper tube, as shown in Fig. 3. Both boundary conditions have a constant heat flux in axial direction, due to the design of the test section.

Due to azimuthal heat conduction in the tube wall, the heat flux distribution changes at the inner surface of the inhomogeneously heated tube. The nominal heat flux density for the inhomogeneous case is specified with respect to half of the inner circumference

$$\dot{q}_{\mathrm{W,IH}} = \frac{\dot{Q}_{\mathrm{res}}}{L_{\mathrm{heat}} \cdot \pi \cdot \frac{D}{2}} \tag{1}$$

where $\dot{Q}_{\mathrm{res}}$ is the resulting heat rate to the flowing metal (see eq. (4)). In order to prevent effects by mixed convection, the inhomogeneous cases are only performed with a top heated wall.

2.4. Data acquisition

All thermocouples in the test section are connected to a thermocouple reference unit (Isotech TRU Model 937), which is attached to isolated measurement pods (Solartron mobrey IMP 3595 1C). Uncertainties due to the calibration and the entire measuring chain were addressed in an uncertainty analysis (see Section 2.5). Flow meters, pressure sensors and facility thermocouples are directly connected to the Siemens PLC control system. All data streams are illustrated in Fig. 4.

2.5. Uncertainty analysis

To consider the extended measurement uncertainty of every target quantity, an uncertainty analysis based on the method of "Guide to the expression of uncertainty in measurement" (GUM) [26] type B was performed using a coverage factor $c = 2$ with a level of confidence of 95%. Prior to the experimental campaign, all thermocouples were calibrated using a reference thermometer (Isotech SPRT 909L/25/TTI with Isotech milliK). All loose thermocouples were calibrated using a calibration thermostat (Isotech Oceanus-6). The thermocouples soldered in the tube walls and placed in the measuring grids were calibrated using in situ-calibration. The pressure sensors and flow meters are factory-calibrated. The uncertainties of the thermophysical properties (see [24, 25]) were included in the analysis. Indeed, these had the most significant impact on the overall extended measurement uncertainties. In order to illustrate the contribution of the single quantities on the extended measurement uncertainty of the circumferentially
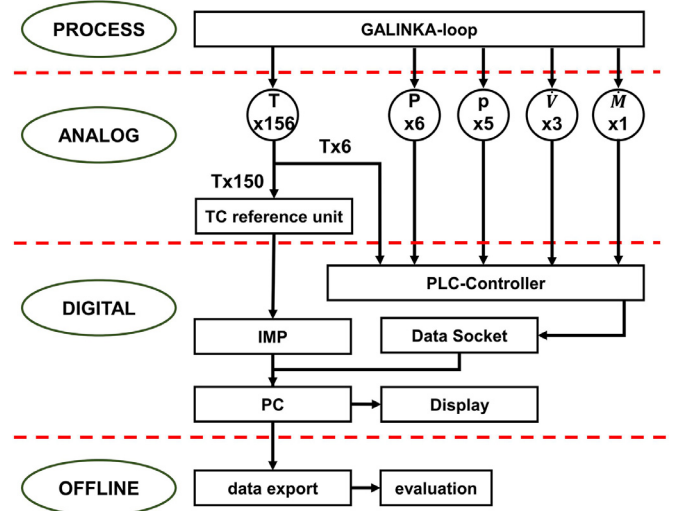

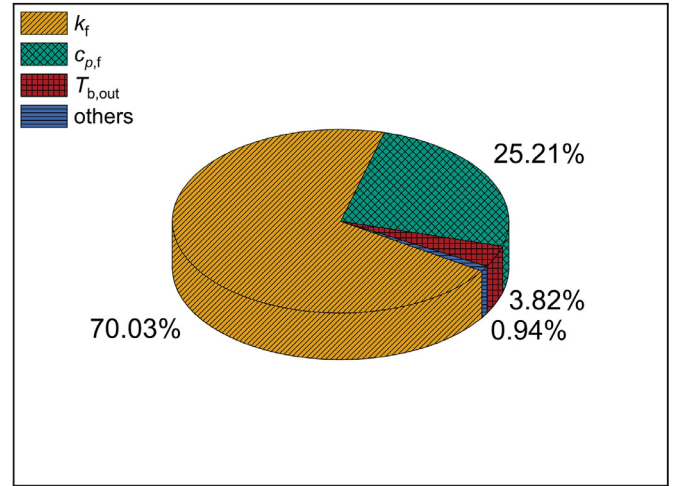**Fig. 4.** Visual representation of the data streams in the data acquisition system

Fig. 5. Illustration of the uncertainty contributions of the input quantities on Nu (OH, measurement plane 3, $\dot{q}_{\mathrm{LM,2}} = 110$ **kW m**$^{-2}$, $Pe = 3600$)

averaged Nusselt number Nu (for the definition see eq. (9)) a characteristic distribution is given in Fig. 5:.

For the sake of clarity, the quantities with the lowest contribution (temperatures in the wall, fluid temperature at the inlet of the test section, geometrical parameters and the mass flow) are summarized in "others". It emerges, that the fluid's thermal conductivity k_{f} and its specific heat capacity at constant pressure $c_{p,\mathrm{f}}$ contribute most to the extended uncertainty of Nu, followed by the fluid temperature at the outlet of the test section $T_{\mathrm{b,out}}$.

3. Data Analysis

All results are presented in dimensionless form using the Reynolds number (Re), the Prandtl number (Pr), the Péclet number (Pe), the Nusselt number (Nu) and a dimensionless temperature of the wall (Θ). For their definition, the reader is referred to the nomenclature. The physical properties are taken at the mean fluid temperature in the test section. The convective heat transfer coefficient h at every axial position z and circumferential position ϕ is calculated as follows:

$$h(\phi, z) = \frac{\dot{q}_{\mathrm{W}}(\phi, z)}{T_{\mathrm{W}}(\phi, z) - T_{\mathrm{b}}(z)} \tag{2}$$

where $\dot{q}_W(\phi, z)$ is the local wall heat flux, $T_W(\phi, z)$ is the local wall temperature and $T_b(z)$ is the local bulk temperature of the fluid. For an axially constant heat flux, $T_b(z)$ can be calculated from an energy balance:

$$T_b(z) = \frac{\dot{Q}_{res}}{\dot{M} \cdot c_p} \frac{z}{L_{heat}} + T_{b,in} \qquad (3)$$

The heat input rate, $\dot{Q}_{res}$, is calculated with the temperature from the measurement grid at the inlet $T_{b,in}$, the temperature behind the static mixing element $T_{b,out}$, the mass flow $\dot{M}$ and the specific heat capacity at constant pressure $c_{p,f}$

$$\dot{Q}_{res} = \dot{M} \cdot c_{p,f} \cdot \left(T_{b,out} - T_{b,in} \right) \qquad (4)$$

For determining the local wall temperature and the local wall heat flux, a distinction between the homogeneous and inhomogeneous case is necessary. For the OH case, the local wall heat flux density on the inner surface of the tube wall is calculated as:

$$\dot{q}_{W,OH} = \frac{\dot{Q}_{res}}{L_{heat} \cdot \pi \cdot D} \qquad (5)$$

Due to azimuthal heat conduction in the wall for the IH case, the heat flux on the inner surface is calculated with the method of Schmidt et al. [8]. According to this, the temperature profile of the thermocouples in the wall $T(\phi)_{TC}$ was approximated using a fourth order Fourier expansion. To determine the local temperature at the inside surface of the wall, the two-dimensional Laplace heat conduction equation in cylindrical coordinates is solved:

$$\frac{1}{r} \frac{\partial}{\partial r} \left(r \frac{\partial T}{\partial r} \right) + \frac{1}{r^2} \frac{\partial^2 T}{\partial \phi^2} = 0 \qquad (6)$$

As the axially temperature gradients are negligible compared to the temperature gradients in radial and azimuthal direction, the problem is handled two-dimensional. A constant heat flux boundary condition is applied at the outer surface of the tube while a constant temperature is applied at the positions of the thermocouples using the approximated temperature profile $T(\phi)_{TC}$:

$$\frac{\partial T}{\partial r} \left(r = r_o, \phi \right) = \frac{\dot{q}_o}{k_{Cu}}; \qquad T\left(r = r_{TC}, \phi \right) = T(\phi)_{TC} \qquad (7)$$

The solution of the differential equation provides the inner wall temperature $T_W(\phi, z)$ at every azimuthal position and at each measurement plane. The inner wall heat flux is then evaluated using Fourier's law and the thermal conductivity of the copper tube k_{Cu}

$$\dot{q}_i = k_{Cu} \cdot \left. \frac{\partial T}{\partial r} \right|_{r=r_i} \qquad (8)$$

This methodology relies on the following assumptions:

- The influence of the thermocouples on the heat transfer in the copper tube is neglected.
- The heat flux on the outside of the copper tube is assumed to be homogeneous within one heating shell.

The validity of this approach was also verified against results from numerical simulations. Differences between simulations and the data analysis were included in the uncertainty analysis. The azimuthally averaged Nusselt number is defined as:

$$Nu = \frac{\dot{q}_W(\phi, z) \cdot D}{\left(T_W(\phi, z) - T_b(z) \right) \cdot k_f} \qquad (9)$$

To enable a comparison of the wall temperature between the different cases, a nondimensional temperature Θ, similar to the one presented by Schmidt et al. [8], is used:

$$\Theta = \frac{T_W(\phi, z) - T_b(z)}{< T_W(\phi, z) > - T_b(z)} \qquad (10)$$
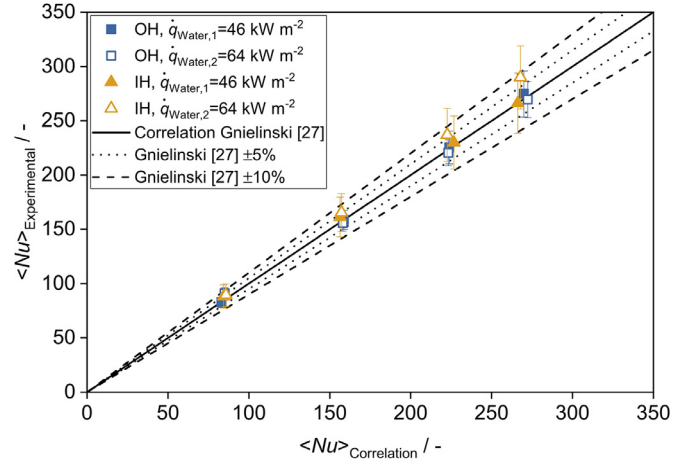

Fig. 6. Parity plot of **Nu** for water experiments and Gnielinski's [27] correlation for OH and IH and different heat flux values

The definition of Θ results in a theoretical value of one for homogeneous heating, when the differences in local wall temperature are negligibly small. For inhomogeneous heating, Θ becomes larger than one on the heated side and smaller than one on the unheated side. The definition of the angular position in the wall ϕ corresponds to the one shown in Fig. 3.

To quantify the differences between the experimental results and a reference, e.g. an empirical correlation, the mean absolute percentage error (MAPE) is used

$$MAPE = \frac{100}{n} \sum_{i=1}^{n} \left| \frac{x_{ref} - x_1}{x_{ref}} \right| \qquad (11)$$

where x_1 is an arbitrary quantity and x_{ref} is the corresponding reference quantity.

4. Results and discussion

4.1. Operation with water

4.1.1. Experimental operating conditions

Water experiments were performed to validate the test section with existing literature correlations. For this purpose, the test section was connected to the primary cooling water loop to use the built-in pump to achieve a maximal volume flowrate of $\dot{V}_{Water} = 1.8$ m^3 h^{-1}. The secondary cooling water loop was linked to the primary loop via a plate heat exchanger to remove a heat rate up to $P_{Water,max.} = 5$ kW. Two different nominal heat flux values of $\dot{q}_{Water, 1} = 46$ kW m^{-2} and $\dot{q}_{Water, 2} = 66$ kW m^{-2}, were applied for both the homogeneous and inhomogeneous case. The Reynolds number could be varied between $Re_{Water} = 10000, 20000, 30000, 37000$ through a by-pass. The Prandtl number of water exhibits a pronounced temperature dependency and varied on average between 2.2% and a maximum of 8.1% from the reference value of $Pr_{Water} = 7.3$. In the following section, all data points are taken at the third measurement plane, 60 hydraulic diameters behind the start of the heated section in order for the water flow to be thermally fully developed.

4.1.2. Experimental results and comparison with Gnielinski's correlation

The experimental results of Nu for both homogeneous and inhomogeneous heating are shown Fig. 6. The data are compared with Gnielinski's [27] correlation, which is valid for turbulent water flows with $4 \cdot 10^3 < Re < 10^6$. The numerical values of Nu and the respective uncertainties, are listed in Appendix B (see
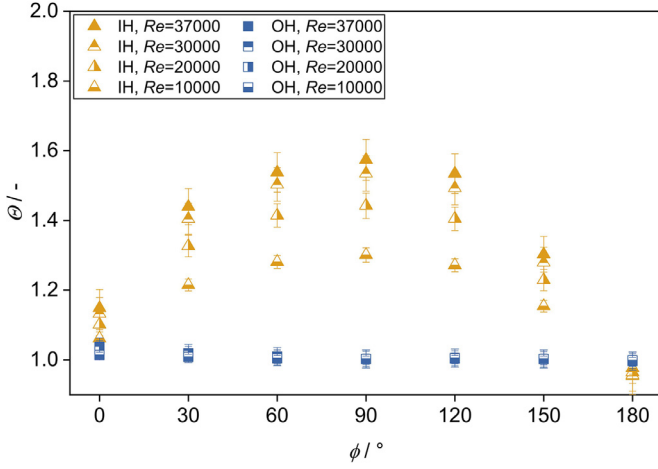
Fig. 7. Nondimensional temperature distribution Θ on the heated side as function of angular position ϕ for OH and IH at different **Re** and $\dot{q}_{\text{Water},1} = 46$ **kW m^{-2}**

Fig. 8. Nondimensional temperature distribution Θ on the unheated side as function of angular position ϕ for OH and IH at different **Re** and $\dot{q}_{\text{Water},1} = 46$ **kW m^{-2}**

Tables 2 and 3). The maximal deviation from Gnielinski's [27] correlation for the OH is 7.2% with a MAPE of 1.7%. For the IH, the maximal deviation is 8.3% with a MAPE of 4.1%. Due to the minor deviations of the homogeneous cases from Gnielinski's [27] correlation, the experimental data are considered to be highly trustworthy. As expected for a single phase flow in the regime of forced convection, the results are independent from the heat flux. A comparison between OH and IH shows that no considerable differences arise for Nu. Consequently, Gnielinski's [27] correlation is very well suited to predict azimuthally averaged Nusselt numbers for both azimuthally homogeneous and inhomogeneous heated turbulent tube water flow. These observations are also in good agreement with the results of Schmidt et al. [8].

In Fig. 7, the nondimensional temperature distribution Θ (eq. (10)) on the solid-fluid surface of the heated wall is plotted over the angular position ϕ and at different Reynolds numbers. For reasons of clarity, only the data points for one heat flux value are shown, as no significant influence of the heat flux on the nondimensional temperature could be identified.

For the OH, the maximum relative uncertainty of Θ is 2.6% with a mean value of 1.8%. For the IH, the relative uncertainties are slightly higher with a maximum and mean value of 5.6% and 3% respectively. It is evident that for the OH the nondimensional temperature is equal to one, irrespective of the Reynolds number. Because of small inequalities of the heaters, the temperature distribution shows small deviations along the perimeter. For the IH, the temperature distribution takes a sine-like shape due to azimuthal heat conduction in the wall. Again, the distribution is slightly asymmetrical, especially at $\phi = 0°$ and $\phi = 180°$, because of non-perfect heating. In contrast to the OH, the data indicates a pronounced influence of the Reynolds number on Θ. Increasing the Reynolds number results in higher differences between Θ_{min} and Θ_{max}. It is worth noting here that higher values of Re correspond to lower wall temperatures but higher values of Θ, the latter corresponding to the local excess temperature over the mean value. The distribution of Θ on the unheated side of the wall is shown in Fig. 8.

For the OH the maximal relative uncertainty of Θ is 2.7% with a mean value of 1.8%. For the IH the relative uncertainties are slightly higher with a maximal and mean value of 16.1% and 6% respectively. Analogous to the temperature distribution on the heated side, the values of Θ deviate more from unity as Re increases. For all investigated Reynolds numbers, Θ was always larger than zero, corresponding to a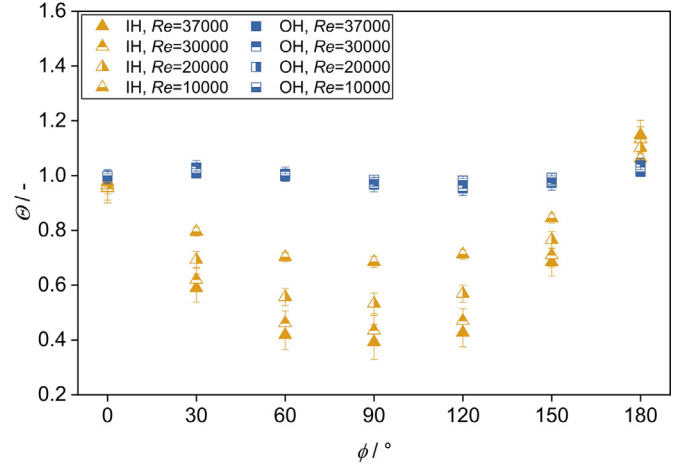 wall temperature always higher than the bulk temperature at every azimuthal position, due to azimuthal heat conduction in the tube wall.

4.2. Operation with GaInSn

4.2.1. Experimental operating conditions

Analogous to the water experiments, two nominal heat flux values, namely $\dot{q}_{\text{LM},1} = 83$ kW m^{-2} and $\dot{q}_{\text{LM},2} = 110$ kW m^{-2}, were applied for OH and IH, respectively. For liquid metal heat transfer the Péclet number is commonly used in the Nusselt correlations. The Prandtl number of GaInSn only exhibit a weak temperature dependence compared to water. The variation of the mean Prandtl number was on average 1% and maximum 3% from the reference value of GaInSn $Pr_{\text{LM}} = 0.033$. Seven different Reynolds number values in the range $4.4 \cdot 10^4 < Re < 1.07 \cdot 10^5$ were applied, resulting in Péclet numbers of $Pe = 1400, 1800, 2200, 2500, 2900, 3200, 3600$. To avoid mixed convection effects, the criterion proposed by Buhr et al. [1] was adopted (eq. (12)).

$$Z = \frac{Ra_{\text{LM}}}{Re_{\text{LM}}} \cdot \frac{D}{L} < 2 \cdot 10^{-3} \tag{12}$$

The maximum value of Z for the experiments of this work was $Z_{\text{max}} = 2.9 \cdot 10^{-5}$. In the following section, all data points are taken at the third measurement plane, in the same way as for the water experiments.

4.2.2. Experimental results and comparison with Skupinski's correlation

The experimental results for the azimuthally averaged Nusselt number Nu for OH are compared to the correlation of Skupinski et al. [14] in Fig. 9. The differences in Nu between $\dot{q}_{\text{LM},1}$ and $\dot{q}_{\text{LM},2}$ are marginal and smaller than the uncertainties of the measurements. For the numerical values of the Nusselt number and the respective uncertainties the reader is referred to Appendix B (see Table 4). Skupinski's correlation [14] slightly overestimates the experimental data for the entire range of the investigated Péclet numbers and shows a constant relative deviation smaller than the specified uncertainty range of $\pm15\%$. The majority of data points fits the correlation even better with a maximal deviation of 9.3% and a MAPE of 6.6 %.

The azimuthally averaged Nusselt numbers Nu determined for OH are compared with those for IH and also with the correlation of Skupinski et al. [14] in Fig. 10. The numerical values of Nu for IH and the respective uncertainties are also given in Appendix B (see Table 5).
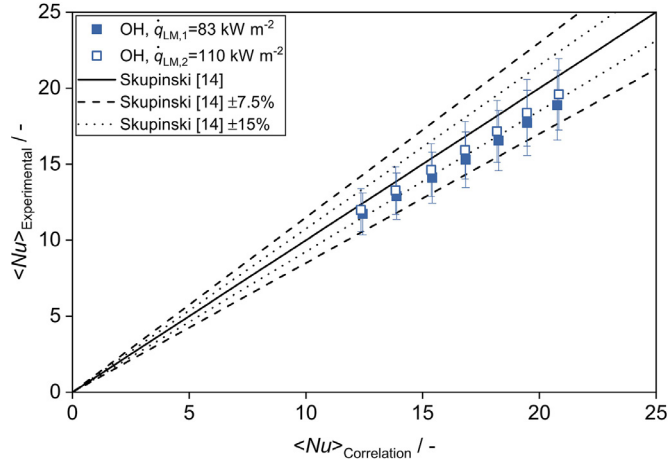
Fig. 9. Comparison of experimental results of Nu for OH and different heat fluxes with Skupinski's [14] correlation
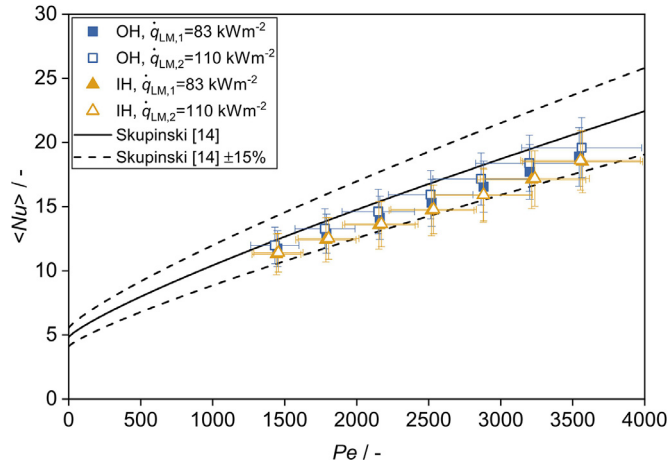

Fig. 10. Experimental results of Nu as a function of Pe for OH and IH for different heat fluxes and Skupinki's [14] correlation

Fig. 11. Nondimensional temperature distribution Θ on the heated side as function of angular position ϕ for OH and IH at different Pe and $\dot{q}_{LM,2} = 110$ **kW m^{-2}**

Fig. 12. Nondimensional temperature distribution Θ on the unheated side as function of angular position ϕ for OH and IH with $\dot{q}_{LM,2} = 110$ **kW m^{-2}**

It can be noted that the thermal boundary condition does not significantly affects Nu. This observation agrees well with the findings of Marocco et al. [7] (numerical simulation) and Melnikov et al. [15] (experiments using Hg). Trend-wise, the data for IH are slightly below those for OH. Similar to OH, no significant influence of the heat flux is observed. The deviation of the values for the IH from Skupinski's [14] correlation is maximum 12.9% with a MAPE of 11.4%, which is higher than the values for OH. Anyway, all data points are still within the uncertainty range of ±15% given by Skupinski et al. [14] for their correlation.

To study the local temperature distribution on the heated side of the tube wall, Θ as a function of ϕ is shown in Fig. 11, for both the OH and IH and three Péclet numbers.

As no noteworthy differences are recognisable between the two heat flux values, only the data for $\dot{q}_{LM,2} = 110$ kW m^{-2} are shown. For the homogeneous cases Θ is close to unity. Similar to the water experiments, for the IH the temperature distribution takes a sine-like shape due to the circumferential heat conduction in the wall. Again, the distribution is slightly asymmetrical especially at $\phi = 0°$ and $\phi = 180°$ because of non-perfect heating. The maximal relative uncertainty of Θ is 3.7% with a mean value of 2.6% for the OH. The data of the IH exhibit higher relative uncertainties with a maximal and mean value of 8.2% and 3.7% respectively. Similar to the water results, no big differences arises for the OH at different Péclet numbers. The slight inequal-
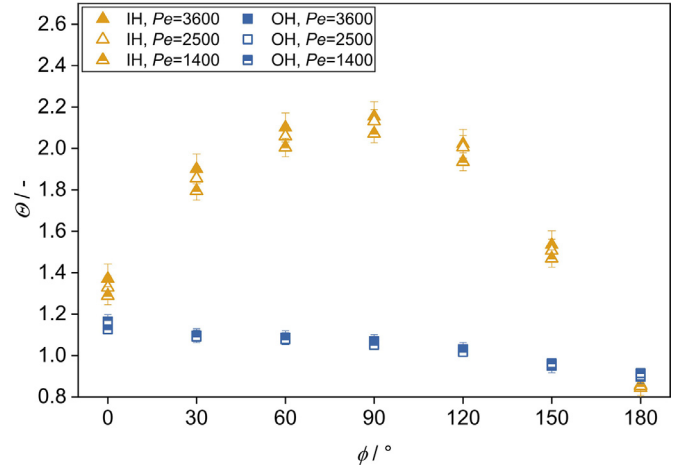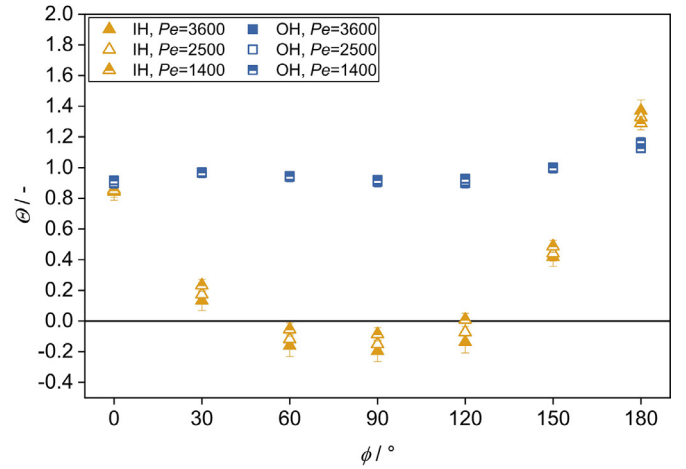
ities of the heaters are more pronounced for the liquid metal experiments, which can be seen from the higher deviation of Θ from unity for the OH. One possible reason can be the much higher convective heat transfer coefficient for liquid metals that eventually compensate the azimuthal heat conduction in the tube wall. Compared to the water experiments, a dependency of Θ from the Péclet number/Reynolds number is recognisable, although it is less pronounced. The convective heat transfer coefficient for the liquid metal flow is high, even at the lowest Péclet number, resulting in higher maximum and minimum values of Θ compared to water.

Fig. 12 depicts the distribution of Θ on the unheated side of the tube wall for $\dot{q}_{LM,2} = 110$ kW m^{-2}. For the OH the nondimensional temperature is close to unity along the perimeter. Slight inequalities of the heaters can be seen and the maximum relative uncertainty is 3.7% with a mean value of 2.8%. For the IH, the nondimensional temperature distribution assumes a sine-like shape due to heat conduction in the tube wall. The minimum values of the nondimensional temperatures on the unheated side are lower compared to the water experiments. Additionally, Θ assumes negative values at $\phi = 90°$ on the unheated side. As the absolute values of Θ for the IH are close to zero, especially for $60° < \phi < 120°$, the relative uncertainties are high. The negative value of Θ indicate that there are zones in the tube wall, where the local wall temperature is lower or equal to the local fluid bulk temperature. Similar observations have been reported by Melnikov

et al. [15]. This circumstance does not necessarily correspond to a heat flux from the fluid to the wall, as for this the fluid temperature close to the wall must be higher than the wall temperature. Unfortunately, the near-wall fluid temperature could not be measured with our experimental setup. Nevertheless, this finding suggests that for a case with a very high convective heat transfer coefficient, a heat flux from the fluid to the wall could be possible.

4.2.3. Influence of impurities on the heat transfer

The data of a first measurement campaign were slightly lower than available literature data. One possible explanation could be the presence of impurities in the liquid metal, which would impair the heat transfer. As the liquid metal coming from the storage tank was filtered during the filling process of the loop, impurities or air could only enter during maintenance, when the loop was open to the environment. Ivanovskii et al. [28] reported that impurities in a turbulent lithium flow have a negative impact on the heat transfer, due to their accumulation in the thermal boundary layer. Their lower thermal conductivity results in a local decrease of the fluid's thermal conductivity and therefore reduces the heat transfer coefficient.

Oxides and impurities can be removed by mechanical filtering when flushing the loop. Therefore, multiple heat transfer experiments were conducted without flushing, with a flushing time of 20 minutes and a flushing time of 8 hours. The flushing was done prior to the experiments using the bypass-filter. As the differences between the flushing of 20 minutes and 8 hours were marginal, only the latter results are presented. In Fig. 13, the circumferentially averaged Nusselt number is plotted over the Péclet number for $\dot{q}_{LM,1}$ = 83 kW m^{-2} together with different Nusselt number correlations developed for liquid metals.

The influence of liquid metal flushing and thus the removal of the impurities is evident. If the latter are present under otherwise identical experimental conditions, a significant lower Nu is obtained compared to the clean liquid metal. The uncertainties for Nu and the Péclet number before and after the flushing process were practically identical. The maximal and mean relative uncertainty for Nu was 12.1% and 12%, for the Péclet number the relative uncertainty was constant with a mean value of 11.7%. It should be noted though that no quantitative analysis of the oxide particle content could be conducted, i.e. all results have to considered as qualitative.

Furthermore, the experimental results are compared to well established liquid metal correlations from literature. The correlation of Kutateladze et al. [30], recommended for Hg-flows, and the cor-

relation of Lubarsky and Kaufmann [32], recommended for Pb and flows of lead-bismuth-eutectic (LBE), fit the experimental Nu values comparably well for the case without flushing, i.e., in the presence of oxide particles. The experimental data are slightly overestimated by the correlations. If the oxide particles are removed from the system, the values of Nu increase significantly and are thus underestimated by the correlations just mentioned. For the present case, the correlations of Chen and Chiou [31], recommended for Na and NaK, and the correlation of Skupinski et al. [14], recommended for all classes of liquid metals, seem to be better suited. Additionally, the well-known semi-analytical correlation by Lyon [29] is added to the plot to show the upper Nu values. In practice, it is complicated to control the oxygen content of the flow in large technical facilities [6], so that oxide particles can form and thus impair the heat transfer. The results indicate that the correlation of Skupinski et al. [14] is the one most suited to fit the experimental data of this work. All results presented in Section 4.2.2 were achieved after careful flushing, i.e. with presumably minimum oxide particle load within the fluid.

5. Conclusions

In this work, the results of heat transfer experiments in a turbulent GaInSn tube flow with azimuthally homogeneous and inhomogeneous heating are presented. The test setup was validated using water. The results corresponding for homogeneous and inhomogeneous heat flux showed very good agreement with literature data. They were compared to the liquid metal results in order to analyze the differences between low-Prandtl and common fluids.

The main findings of this work can be summarized as follows:

- No influence of the thermal boundary condition (azimuthally homogeneous or inhomogeneous heating with axially constant heat flux) or of the heat flux on the azimuthally averaged Nusselt number could be identified for both to water and liquid metal flow. Consequently, correlations for homogeneous heating can also be applied to predict the azimuthally averaged Nusselt number for the inhomogeneous case.
- The data for the azimuthally averaged Nusselt number of the liquid metal flow showed the best accordance with Skupinski's [14] correlation. Therefore, this correlation is recommended for turbulent tube flows of GaInSn. However, a systematic overestimation of the experimental data by Skupinski's [14] correlation was detected. Consequently, an adaption of the correlation may be possible in the future based on a larger data set.
- The azimuthal temperature gradients in the tube wall for the inhomogeneous heat flux are much higher for GaInSn than for water. This has to be considered when designing technical equipment using low-Prandtl number fluids e.g. the receiver of a CSP system [33].
- Particulate impurities like metal oxides may have a big influence on the convective heat transfer coefficient in a turbulent liquid metal flow. By applying mechanical filtering a substantial improvement in the heat transfer could be achieved.

Declaration of Competing Interest

no conflicts of interest exist.

CRediT authorship contribution statement

Tim Laube: Conceptualization, Methodology, Software, Validation, Formal analysis, Investigation, Resources, Data curation, Writing – original draft, Writing – review & editing, Visualization. **Benjamin Dietrich:** Supervision, Project administration, Funding acquisition, Writing – review & editing. **Luca Marocco:** Supervision, Funding acquisition, Writing – review & editing. **Thomas**
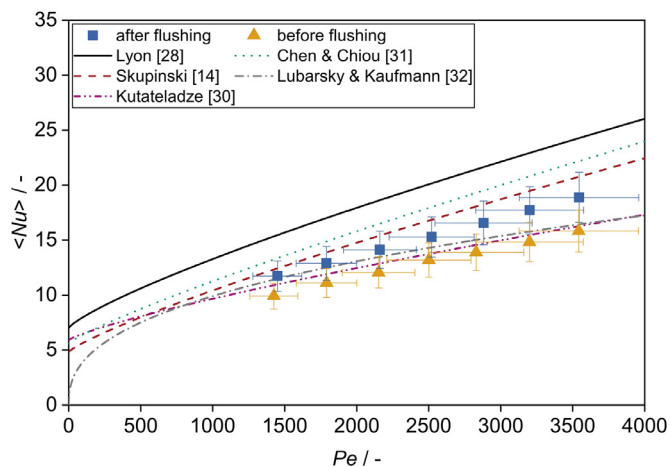

Fig. 13. Comparison of experimental results for **Nu** with literature data [14, 29–32] for OH with $\dot{q}_{LM,1}$ = 83 **kW m**$^{-2}$ before and after flushing of the flow

Appendix A

Flow Measurements

The flow measurements in the liquid metal loop are conducted using two different measuring principles, a magnetic-inductive flow meter (MID) and a coriolis flow meter (see Section 2.2). The use of magnetic-inductive flowmeters in liquid metal flows might lead to severe errors because the sensor's electrodes are usually poorly wetted by heavy metals [6]. To the author's best knowledge, these investigations were not reported for GaInSn as working fluid yet. Therefore, two sensors with different measurement principles are used in the test section. They are placed in series with enough distance from each other in consideration of the hydrodynamic inlet and outlet lengths. The signal of the magnetic-inductive flow meter corresponds to the flow velocity u, while the output signal of the coriolis flow meter is related to the mass flow $\dot{M}$. Therefore, the signal of the magnetic-inductive flow meter has to be converted to a mass flow using the temperature dependent density of the liquid metal ρ_f and the cross-sectional area of the tube A.

$$\dot{M} = u \cdot A \cdot \rho_f \tag{13}$$

During the measurements, the temperature of the fluid was kept constant at a value of $T = 24\ °C \pm 2\ K$ to eliminate influences of large temperature gradients on the experiments. The results for the mass flow determined by each sensor are plotted in Fig. 14.

The difference between the two sensors is marginal in the entire measuring range of 2800 kg h^{-1} to 10050 kg h^{-1}. The MAPE of both signals is 0.24% with a maximal deviation of 0.42%. The relative measurement uncertainties of both sensors are covered by the symbols in Fig. 14. The uncertainties related to the coriolis flow meter have a mean value of 0.8% of the measured quantity and a maximal value of 1.5% at the lowest mass flow. The relative uncertainties of the magnetic-induced sensor were slightly higher with a
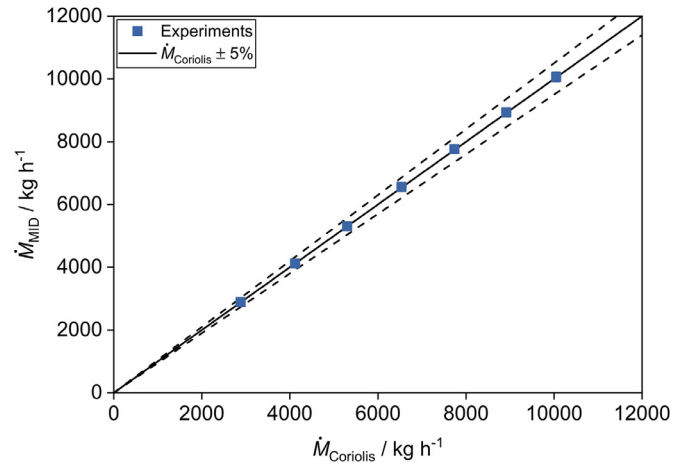

Fig. 14. Comparison of experimental results for the different flow sensors

mean and maximal value of 2.4% and 4.2% respectively. The results presented in this work are a first indication that magnetic-induced flow sensors can be used for GaInSn flows. However, the extent of this investigation is still limited and should be further enlarged concerning sensors of other manufacturers, temperatures as well as mass flows.

Appendix B

In the following sections, selected results of this work are summarized with the corresponding uncertainties of the quantities.
Results water experiments
Results liquid metal experiments

Table 4
Results of liquid metal experiments and homogeneous heating

$\dot{q}_{LM,1}$ = 83 kW m^{-2}				$\dot{q}_{LM,2}$ = 110 kW m^{-2}			
Pe	U_{Pe}	Nu	U_{Nu}	Pe	U_{Pe}	Nu	U_{Nu}
3544	414	18.88	2.29	3562	417	19.59	2.34
3201	374	17.72	2.14	3199	374	18.38	2.19
2881	337	16.55	1.99	2864	335	17.16	2.04
2520	295	15.29	1.83	2514	294	15.92	1.89
2161	253	14.12	1.68	2150	252	14.61	1.73
1790	210	12.9	1.53	1779	209	13.26	1.57
1449	170	11.73	1.39	1431	168	11.98	1.41

Table 2
Results of water experiments and homogeneous heating

$\dot{q}_{Water,1}$ = 46 kW m^{-2}						$\dot{q}_{Water,2}$ = 64 kW m^{-2}					
Re	U_{Re}	Pr	U_{Pr}	Nu	U_{Nu}	Re	U_{Re}	Pr	U_{Pr}	Nu	U_{Nu}
37435	1211	7.46	0.26	275	21.2	37777	1222	7.39	0.26	269	16.5
30244	994	7.41	0.26	225	15.1	30089	991	7.32	0.25	221	11.9
20430	733	7.3	0.25	159	8.7	20297	733	7.17	0.25	156	7.5
9995	499	6.98	0.24	83	4.7	10293	515	6.73	0.23	91	5

Table 3
Results of water experiments and inhomogeneous heating

$\dot{q}_{Water,1}$ = 46 kW m^{-2}						$\dot{q}_{Water,2}$ = 64 kW m^{-2}					
Re	U_{Re}	Pr	U_{Pr}	Nu	U_{Nu}	Re	U_{Re}	Pr	U_{Pr}	Nu	U_{Nu}
36829	1192	7.59	0.26	266	27.7	37123	1201	7.52	0.26	299	29
30697	1004	7.54	0.26	230	24.5	30064	987	7.47	0.26	237	24.5
20146	722	7.45	0.26	161	18.2	20248	726	7.39	0.26	166	17.4
10161	491	7.31	0.25	88	10.8	10329	499	7.18	0.25	89	10.4

Table 5
Results of liquid metal experiments and inhomogeneous heating

$\dot{q}_{LM,1}$ = 83 kW m^{-2}				$\dot{q}_{LM,2}$ = 110 kW m^{-2}			
Pe	U_{Pe}	Nu	U_{Nu}	Pe	U_{Pe}	Nu	U_{Nu}
3569	417	18.5	2.41	3554	416	18.61	2.32
3215	376	17.11	2.26	3237	379	17.19	2.17
2878	337	15.89	2.12	2882	337	15.91	2.02
2519	295	14.7	1.99	2534	297	14.78	1.9
2154	252	13.54	1.85	2171	254	13.64	1.77
1786	209	12.41	1.72	1805	211	12.51	1.64
1443	169	11.28	1.59	1457	171	11.41	1.51

References

[1] H.O. Buhr, A.D. Carr, R.E. Balzhiser, Temperature profiles in liquid metals and the effect of superimposed free convection in turbulent flow, Int. J. Heat Mass Transfer 11 (4) (1968) 641–654, doi:10.1016/0017-9310(68)90067-7.

[2] N. Lorenzin, A. Abánades, A review on the application of liquid metals as heat transfer fluid in Concentrated Solar Power technologies, Int. J. Hydrogen Energy 41 (17) (2016) 6990–6995, doi:10.1016/j.ijhydene.2016.01.030.

[3] J. Pacio, C. Singer, T. Wetzel, R. Uhlig, Thermodynamic evaluation of liquid metals as heat transfer fluids in concentrated solar power plants, Appl. Therm. Eng. 60 (1-2) (2013) 295–302, doi:10.1016/j.applthermaleng.2013.07.010.

[4] A. Fritsch, An analysis of potential of solar tower power plants using liquid metals as heat transfer fluid, doctoral thesis, Rheinisch-Westfälische Technische Hochschule Aachen, Aachen, Germany (2018).

[5] F. Müller-Trefzer, K. Niedermeier, F. Fellmoser, J. Flesch, J. Pacio, T. Wetzel, Experimental results from a high heat flux solar furnace with a molten metal-cooled receiver SOMMER, Sol. Energy 221 (2021) 176–184, doi:10.1016/j.solener.2021.03.066.

[6] OECD/NEA, Handbook on lead-bismuth eutectic alloy and Lead properties, materials compatibility, thermalhydraulicsand technologies: OECD/NEA Nuclear Science Committee Working Party on Scientific Issues of the Fuel Cycle Working Group on Lead-bismuth, Eutectic, 2015.

[7] L. Marocco, G. Cammi, J. Flesch, T. Wetzel, Numerical analysis of a solar tower receiver tube operated with liquid metals, Int. J. Therm. Sci. 105 (2016) 22–35, doi:10.1016/j.ijthermalsci.2016.02.002.

[8] R.R. Schmidt, E.M. Sparrow, Turbulent flow of water in a tube with circumferentially nonuniform heating, with or without buoyancy, J. Heat Transfer 100 (3) (1978) 403–405, doi:10.1115/1.3450822.

[9] C. Chang, X. Li, Q.Q. Zhang, Experimental and numerical study of the heat transfer characteristics in solar thermal absorber tubes with circumferentially non-uniform heat flux, Energy Procedia 49 (2014) 305–313, doi:10.1016/j.egypro.2014.03.033.

[10] A.W. Black, E.M. Sparrow, Experiments on turbulent heat transfer in a tube with circumferentially varying thermal boundary conditions, J. Heat Transfer 89 (3) (1967) 258–268, doi:10.1115/1.3614375.

[11] G.R. Knowles, E.M. Sparrow, Local and average heat transfer characteristics for turbulent airflow in an asymmetrically heated tube, J. Heat Transfer 101 (4) (1979) 635–641, doi:10.1115/1.3451049.

[12] X. Yang, X. Yang, J. Ding, Y. Shao, H. Fan, Numerical simulation study on the heat transfer characteristics of the tube receiver of the solar thermal power tower, Appl. Energy 90 (1) (2012) 142–147, doi:10.1016/j.apenergy.2011.07.006.

[13] J. Pacio, L. Marocco, T. Wetzel, Review of data and correlations for turbulent forced convective heat transfer of liquid metals in pipes, Heat Mass Transfer 51 (2) (2015) 153–164, doi:10.1007/s00231-014-1392-3.

[14] E. Skupinski, J. Tortel, L. Vautrey, Determination des coefficients de convection d'un alliage sodium-potassium dans un tube circulaire, Int. J. Heat Mass Transfer 8 (6) (1965) 937–951, doi:10.1016/0017-9310(65)90077-3.

[15] I.A. Melnikov, E.V. Sviridov, V.G. Sviridov, N.G. Razuvanov, Experimental investigation of MHD heat transfer in a vertical round tube affected by transverse magnetic field, Fusion Eng. Des. 112 (5) (2016) 505–512, doi:10.1016/j.fusengdes.2016.06.003.

[16] I.A. Belyaev, L.G. Genin, Y.I. Listratov, I.A. Melnikov, V.G. Sviridov, E.V. Sviridov, Liquid metal heat transfer specific in a tokamak reactor, Magnetohydrodynamics 49 (2013) 177–190.

[17] I.A. Melnikov, V.G. Razuvanov, V.G. Sviridov, E.V. Sviridov, A.A. Shestakov, An investigation of heat exchange of liquid metal during flow in a vertical tube with non-uniform heating in the transverse magnetic field, Therm. Eng. 60 (5) (2013) 355–362.

[18] S. Straub, P. Forooghi, L. Marocco, T. Wetzel, B. Frohnapfel, Azimuthally inhomogeneous thermal boundary conditions in turbulent forced convection pipe flow for low to medium Prandtl numbers, Int. J. Heat Fluid Flow 77 (6) (2019) 352–358, doi:10.1016/j.ijheatfluidflow.2019.05.003.

[19] N.B. Morley, J. Burris, L.C. Cadwallader, M.D. Nornberg, GaInSn usage in the research laboratory, Rev. Sci. Instrum. 79 (5) (2008) 56107, doi:10.1063/1.2930813.

[20] P. Geddis, L. Wu, A. McDonald, S. Chen, B. Clements, Effect of static liquid Galinstan on common metals and non-metals at temperatures up to 200°C, Can. J. Chem. 98 (12) (2020) 787–798, doi:10.1139/cjc-2020-0227.

[21] W.R. Hunter, R.T. Williams, Grain boundary diffusion of liquid metal coolants in optical materials for use with high power synchrotron radiation, Nucl. Instrum. Methods. Phys. Res. A 222 (1984) 359–363.

[22] H. Kolb, R. Sottong, T. Dasgupta, E. Mueller, J. de Boor, Evaluation of detachable ga-based solder contacts for thermoelectric materials, J. Elec. Mater. 46 (8) (2017) 5057–5063, doi:10.1007/s11664-017-5486-9.

[23] T. Liu, P. Sen, C.-J. Kim, Characterization of nontoxic liquid-metal alloy galinstan for applications in microdevices, J. Microelectromech. Syst. 21 (2) (2012) 443–450, doi:10.1109/JMEMS.2011.2174421.

[24] Y. Plevachuk, V. Sklyarchuk, S. Eckert, G. Gerbeth, R. Novakovic, Thermophysical properties of the Liquid Ga–In–Sn eutectic alloy, J. Chem. Eng. Data 59 (3) (2014) 757–763, doi:10.1021/je400882q.

[25] T. Laube, F. Emmendörfer, B. Dietrich, L. Marocco, T. Wetzel, Thermophysical properties of the near eutectic liquid Ga-In-Sn alloy, KITopenData [Online-database] (2021), doi:10.5445/IR/1000140052.

[26] Guide to the Expression of Uncertainty in Measurement (GUM), International Organization for Standardization, 1993.

[27] V. Gnielinski, On heat transfer in tubes, Int. J. Heat Mass Transfer 63 (2013) 134–140, doi:10.1016/j.ijheatmasstransfer.2013.04.015.

[28] M.N. Ivanovskii, Y.I. Orlov, V.I. Subbotin, Thermal conductivity of the boundary layer in liquid-metal coolant flow, Atomnaya Énergiya 22 (3) (1967) 231–233.

[29] R.N. Lyon, Liquid metal heat-transfer coefficients, Chem. Eng. Prog. 47 (2) (1951) 75–79.

[30] S.S. Kutateladze, V.M. Borishanskii, I.I. Novikov, Heat transfer in liquid metals, Soviet J. Atomic Energy 4 (5) (1958) 555–571.

[31] C.-J. Chen, J.S. Chiou, Laminar and turbulent heat transfer in the pipe entrance region for liquid metals, Int. J. Heat Mass Transfer 24 (7) (1981) 1179–1189, doi:10.1016/0017-9310(81)90167-8.

[32] B. Lubarsky, S.J. Kaufman, Review of experimental investigations of liquid-metal heat transfer 1270 (1956).

[33] J. Flesch, LBE-cooled tube receiver performance - Design aspects and high-flux operation in a solar furnace, doctoral thesis, Karlsruhe Institute of Technology, Karlsruhe, Germany (2021).